Available online at www.sciencedirect.com

SciVerse ScienceDirect

Procedia IUTAM 00 (2012) 000-000

Procedia IUTAM

www.elsevier.com/locate/procedia

Topological Fluid Dynamics II

Three-dimensional vorticity configurations in miscible Hele-Shaw displacements

Rafael M. Oliveira[a], Eckart Meiburg[b,*]

[a]*Instituto de Matemática Pura e Aplicada, Estrada Dona Castorina 110, Rio de Janeiro, RJ 22460-320, Brazil*
[b]*Department of Mechanical Engineering, University of California at Santa Barbara, Santa Barbara, CA 93106, USA*

Abstract

Three-dimensional Navier-Stokes simulations of unstable, miscible displacements in Hele-Shaw cells are discussed. In neutrally buoyant flows, the formation of streamwise vorticity quadrupoles is shown to result in the formation of a novel inner splitting mechanism. In the presence of density differences, the interaction of these quadrupoles with a Rayleigh-Taylor instability can lead to the formation of an 'anchor'-like structure in vertical displacements. Gravitational effects in horizontal displacements break the up/down symmetry of the flow and result in streamwise vorticity dipoles that can split the finger lengthwise.

Keywords: Navier-Stokes simulations; three-dimensional; Hele-Shaw cell; streamwise vorticity; inner splitting

1. Introduction

Viscous fingering can evolve when a more viscous fluid is displaced by a less viscous one in a Hele-Shaw cell. This hydrodynamic instability, which has been under investigation for over fifty years ([1, 2, 3]), has a number of industrial applications, including oil extraction processes. Due to its similarity to porous media flows, many viscous fingering studies have been undertaken in Hele-Shaw cells, an apparatus that consists of two solid plates separated by a narrow gap. The interfacial evolution of this displacement process is usually modeled by taking an average across the gap of the Hele-Shaw cell and treating the problem as effectively two-dimensional.

In such a two-dimensional description, gapwise vorticity is the only nonzero vorticity component. It drives the finger formation and it has been employed, together with Darcy's law, by Tryggvason & Aref [4] and by Meiburg & Homsy [5] to perform nonlinear simulations of immiscible displacements in a Hele-Shaw cell. Displacements of miscible fluids lack the presence of a sharp interface, and consequently the vortex-sheet formalism cannot be used. Nevertheless, various authors have employed a vorticity formulation of Darcy's law combined with a convection-diffusion equation for the concentration field, to simulate nonlinear miscible fingering growth ([6, 7, 8, 9, 10]).

* Corresponding author. Tel.: +1-805-893-5278 ; fax: +1-805-893-8651 .
E-mail address: meiburg@engineering.ucsb.edu

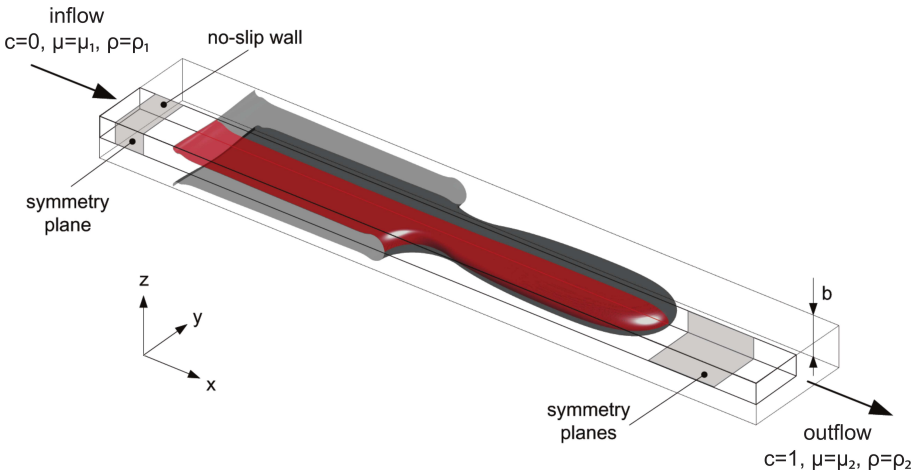

Fig. 1. Schematic representation of the miscible interface between two viscous fluids with viscosities μ_1 (injected) and $\mu_2 > \mu_1$, and densities ρ_1 (injected) and $\rho_2 > \rho_1$. When present, gravity points either in the $-x$ or in the $-z$ direction. In the absence of gravitational effects, or when gravity is aligned with the x-axis, the two planes of symmetry of the problem allow us to restrict the numerical solution to one-quarter of the domain.

Several studies indicate that a three-dimensional description is necessary to obtain quantitative agreement between simulation results and experimental observations. McLean & Saffman [11] calculated the finger width as a function of the capillary number in immiscible displacements. They found only qualitative agreement with the experimental results of Pitts [12] and Saffman & Taylor [2], and suggested that a non-uniform finger thickness may have to be considered to obtain further agreement. More recently, a series of investigations ([13, 14, 15, 16, 17]) analyzed the linear stability of miscible Hele-Shaw fingers against spanwise perturbations based on the three-dimensional Stokes equations. Comparisons with gap-averaged Darcy results indicate that this two-dimensional description overpredicts both the maximum growth rates and the most amplified wave numbers. Very recently, a first set of three-dimensional direct numerical simulations of miscible viscous fingers was published by Oliveira & Meiburg [18]. The authors identified a new interfacial instability that splits the finger lengthwise behind its tip but leaves the front intact. The authors show that this inner splitting mechanism is driven by the presence of the streamwise vorticity component, so that it cannot be captured by a gap-averaged formulation.

In the following, we will analyze how the streamwise vorticity affects the evolution of the interface between two miscible fluids confined in a Hele-Shaw cell. After formulating the problem and its boundary conditions, discretization and validation in section 2, the purely viscous problem will be discussed (section 3) in which both fluids have the same density. Section 4 will include density differences and gravitational effects in both vertical and horizontal displacements, and section 5 summarizes our main findings.

2. Problem formulation

We consider the displacement of a viscous fluid with viscosity μ_2 by a less viscous fluid with viscosity μ_1, miscible with the first, in a Hele-Shaw cell of gap thickness b (see figure 1). The incompressible flow is governed by the three-dimensional Navier-Stokes equations with variable density and viscosity, coupled to a convection-diffusion equation for the concentration field:

$$\frac{\partial u_k}{\partial x_k} = 0\,, \tag{1}$$

$$\frac{\partial u_i}{\partial t} + u_k \frac{\partial u_i}{\partial x_k} = \frac{1}{Re}\left[\frac{\partial}{\partial x_k}\mu\left(\frac{\partial u_i}{\partial x_k} + \frac{\partial u_k}{\partial x_i}\right) - \frac{\partial p}{\partial x_i} - \delta_{i,(1\text{ or }3)} Fc\right]\,, \tag{2}$$

$$\frac{\partial c}{\partial t} + u_k \frac{\partial c}{\partial x_k} = \frac{1}{Pe}\frac{\partial}{\partial x_k}\frac{\partial c}{\partial x_k}\,. \tag{3}$$

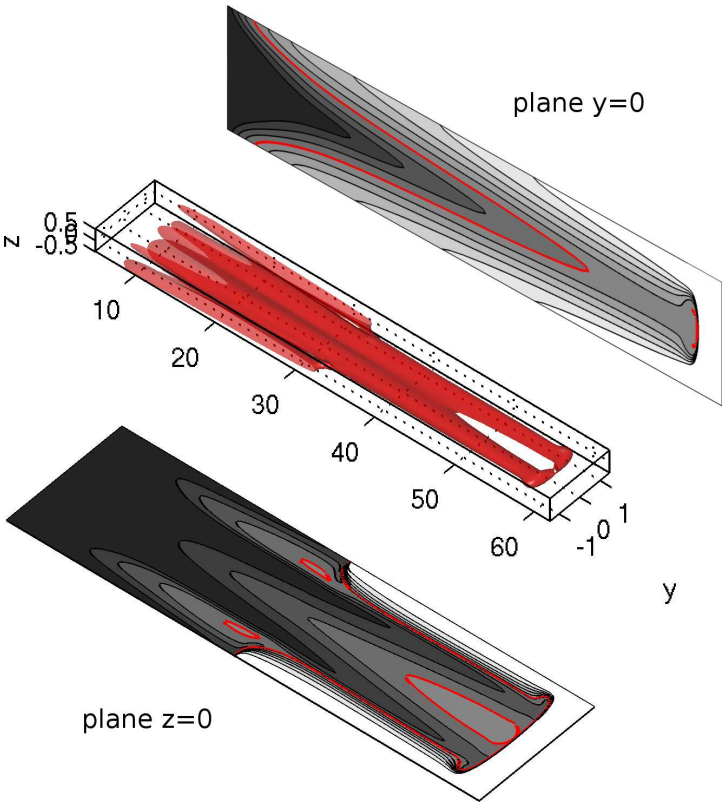

Fig. 2. Perspective view of a viscous finger at time $t = 31$ showing the $c = 0.4$ concentration isosurface in color along with projections of the symmetry planes providing details of the concentration field at the values $c = 0.1, 0.2, \cdots, 0.9$. Darker gray shading corresponds to less viscous fluid. The $c = 0.4$ contour lines are drawn in color in the $y = 0$ and $z = 0$ planes. The governing parameters are $(M, Re, Pe, F) = (3, 1, 1000, 0)$.

In the above set of equations, x_i and u_i represent the Cartesian coordinates and velocity field, respectively, while the viscosity, concentration and pressure fields are given by μ, c and p. All lengths have been scaled by b, velocities by the average inflow Poiseuille velocity U, viscosities by μ_1 and pressure by $\mu_1 U/b$. The viscosity field is related to the concentration field by the exponential function

$$\mu = e^{Mc}, \quad \text{where} \quad \mathrm{M} = \ln \frac{\mu_2}{\mu_1}. \tag{4}$$

Our main governing parameters are the viscosity ratio M, the Reynolds number Re, the Péclet number Pe and the gravitational number F. These last three are defined as

$$Re = \frac{\rho_1 U b}{\mu_1}, \quad Pe = \frac{Ub}{D}, \quad F = \frac{\Delta\rho g b^2}{\mu_1 U}. \tag{5}$$

Re and Pe measure the ratio of advective to diffusive transport of momentum and species, respectively, with D being a constant diffusivity; and F defines the ratio of gravitational to viscous forces, also considered a measure of the density contrast between the fluids.

The discretization of the governing equations is performed using finite differences in a hybrid scheme between a third order Runge-Kutta and a Crank-Nicolson schemes. A factorization approximation is used that allows us to solve only tridiagonal systems of equations in the integration of the diffusive terms, and cosine transformations are employed to solve the Poisson equation for the pressure field. For further details, we point the reader to Oliveira & Meiburg [18].

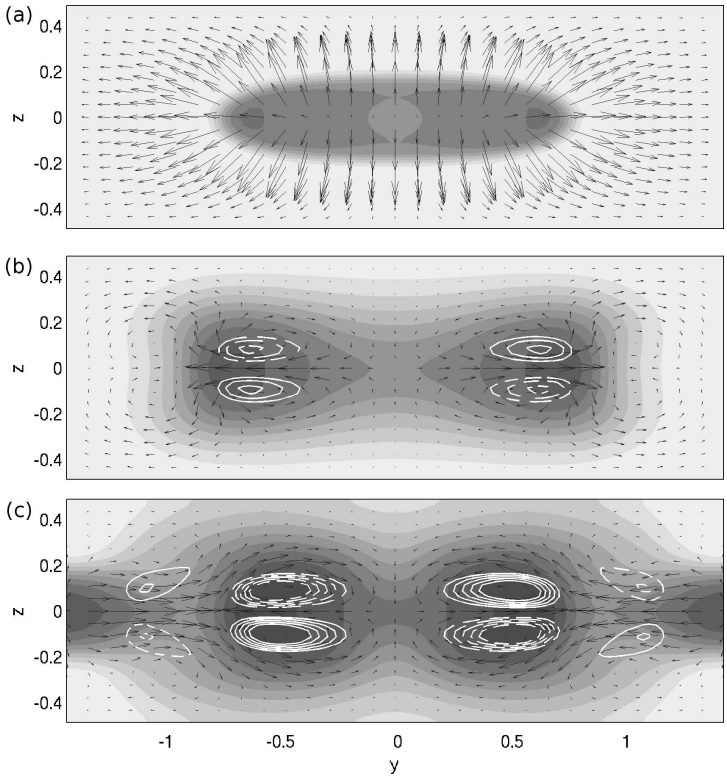

Fig. 3. Cross-section through the locations (a) $x = 59$, (b) $x = 48$ and (c) $x = 32$ for $(M, Re, Pe, F) = (3, 1, 1000, 0)$ at time $t = 31$. Darker gray areas correspond to less viscous fluid. The black arrows indicate the (y,z)-velocity field, and the continuous (dashed) white contours depict positive (negative) streamwise vorticity. The inner vorticity quadrupoles drive fluid from the top and bottom walls to the center of the Hele-Shaw cell, and then displace it laterally in the spanwise direction towards the side boundaries, thus inducing the inner splitting mechanism. This is seen here as pinch-offs of the concentration lines, cf. frame (b).

We validated the numerical implementation by reproducing front thicknesses and tip velocity results of the evolution of the two-dimensional base state, as well as by calculating the linear growth rates predicted by Goyal et al. [14, 15] and by Talon et al. [17] based on their linear stability analyses of the three-dimensional Stokes equations. We obtained generally good agreement with the data of those authors, with errors typically below 2%.

3. Viscous problem

Our simulations will focus on the evolution of a single miscible finger whose spanwise wavelength λ_m is the one of maximum growth as predicted by the linear stability analyses of Goyal et al. [14, 15] and Talon et al. [17]. To generate such a finger, we initialize the flow field by imposing a two-dimensional Poiseuille flow everywhere, along with an error function distribution for the concentration field $c(x,y,z) = 0.5 + 0.5 \cdot \mathrm{erf}\left(\frac{x - x_{\mathrm{init}}}{\delta}\right)$. This two-dimensional state is advanced until the tip reaches a quasisteady configuration around time $t = 2$. At that time, a wavy spanwise perturbation is introduced to trigger the three-dimensional evolution.

In this section, we will focus on the evolution of a viscous finger when both fluids have the same density. Figure 2 shows a perspective view of the $c = 0.4$ concentration isosurface in color, along with projections of the symmetry planes, $y = 0$ and $z = 0$. The contours of the $y = 0$ projection reveal that the thickness of all contours is a decreasing function of the streamwise position x. This suggests that there exists a constant motion of fluid particles from the top and bottom walls towards the midgap plane $z = 0$. As a consequence, an inner splitting mechanism is developed that opens a 'hole' behind the finger tip as shown in the three-dimensional isosurface. The contours in the $z = 0$ plane show that such a splitting has already occurred for values of the concentration smaller then $c = 0.4$, and suggest that

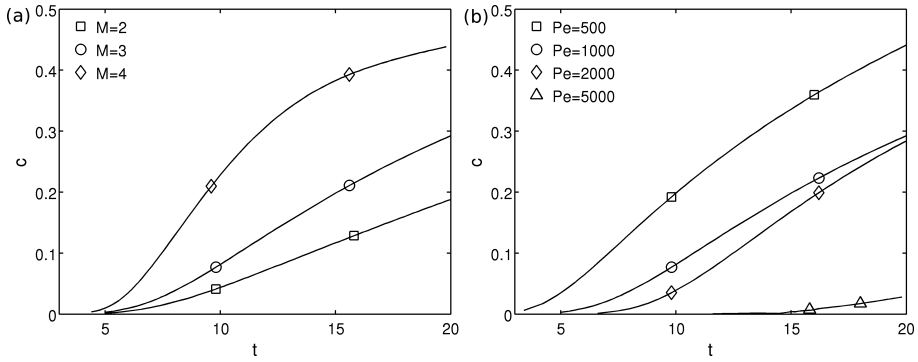

Fig. 4. Value of the concentration field at the moment it undergoes inner splitting as a function of time for (a) constant $Pe = 1000$ and increasing values of $M = 2$, 3 and 4; and for (b) constant M and increasing values of $Pe = 500$, 1000, 2000 and 5000. The inner splitting instability occurs sooner for larger values of the viscosity ratio and smaller values of the Péclet number.

at later times, this concentration value will also split the finger lengthwise. However, the shapes of larger c-values are maintained and their tips remain intact. In fact, we never observed the inner splitting mechanism for concentration values close to or above $c = 0.8$.

Fluid motion from the top and bottom walls towards the midgap plane, and the associated inner splitting instability, occurs due to the presence of the streamwise component of vorticity behind the finger tip. This is shown in figure 3 which depicts streamwise cross-sections through the locations (a) $x = 59$, (b) $x = 48$ and (c) $x = 32$ for the same time and parameters as in figure 2. As before, darker gray contours represent smaller concentration levels and smaller viscosity. The black arrows point in the direction of the projected (y,z)-velocity field, and continuous (dashed) white contours represent positive (negative) streamwise vorticity contours. We realize that in frame (a) the velocity field is similar to a source flow and displaces fluid laterally in all directions. In figure 3(b) we observe a vorticity quadrupole that drives the inner splitting. Here, this instability is observed as pinch-offs of the lines bordering different grays levels. Near the shoulder of the finger, i.e., near the valleys that connect adjacent fingers, the inner quadrupole has increased in magnitude and a second set of streamwise vorticity quadrupoles can be seen.

The influence of the viscosity ratio and of the Péclet number on the inner splitting can be assessed in figure 4, which depicts the value of the concentration field that undergoes the splitting process as a function of time. Figure 4(a) has a fixed Péclet number, $Pe = 1000$, and increasing values of the viscosity ratio, while 4(b) has a fixed viscosity ratio, $M = 3$, and increasing values of the Péclet number. We realize that flows with larger viscosity ratios tend to inner split sooner. The opposite behavior is observed for the Péclet number, i.e., flows with larger Pe tend to inner split later. We remark that we have observed a dual influence of Pe on the inner splitting. While larger diffusivities lead to earlier splittings, the size of the openings are smaller.

4. Buoyancy effects

It is of interest to investigate the situation in which the fluids have different densities as well as different viscosities. This will be done below, for both horizontal and vertical displacements. In these simulations, the injected fluid is lighter and less viscous than the resident, displaced fluid.

4.1. Vertical displacements

Figure 5 shows the $c = 0.35$ concentration isosurface for $(M, Re, Pe, F) = (3, 1, 1000, 20)$ at time $t = 37$. For this concentration value the two different mechanisms to be described below become visible around the same time. For clarity reasons two spanwise wavelengths are depicted, in order to show details of the region connecting two rising fingers. Consequently, the spanwise domain in this figure extends from $-\lambda_m/2$ to $+3\lambda_m/2$.

The flow evolution that results in figure 5 was initialized with a concentration front at $x = 40$. Initially, the interface moves upward until $t \sim 10$. Subsequently the configuration of heavier fluid above lighter fluid triggers a Rayleigh-

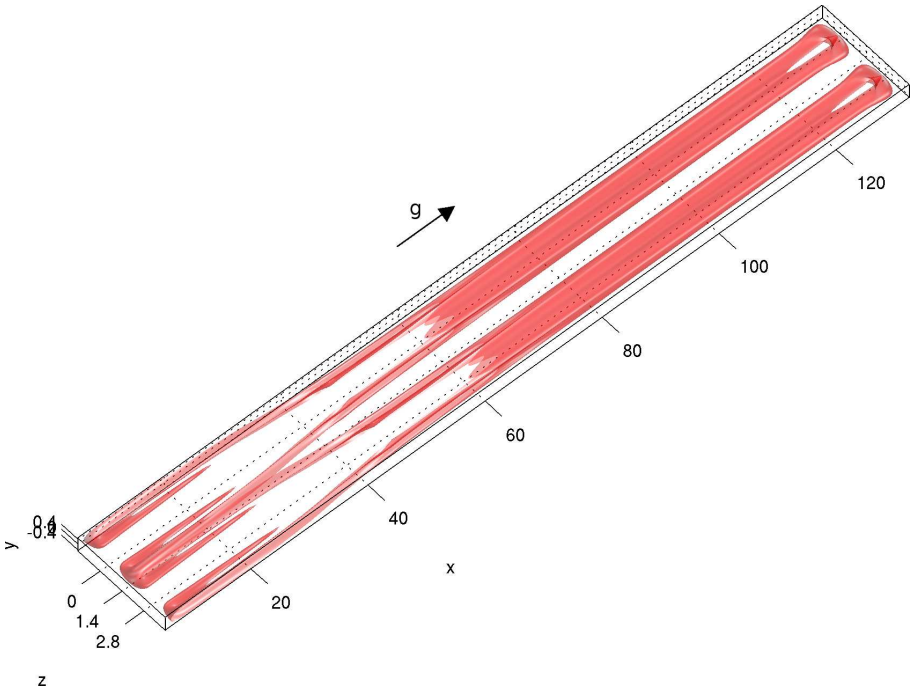

Fig. 5. Three-dimensional perspective view of the $c = 0.35$ concentration isosurface for $(M, Re, Pe, F) = (3, 1, 1000, 20)$ at time $t = 37$. Two spanwise wavelengths are shown for clarity. The upward moving front undergoes an inner splitting event, similar to the neutrally buoyant case discussed earlier. A Rayleigh-Taylor instability combines with the streamwise vorticity quadrupoles to form the 'anchor'-like structure seen in the downward propagating front.

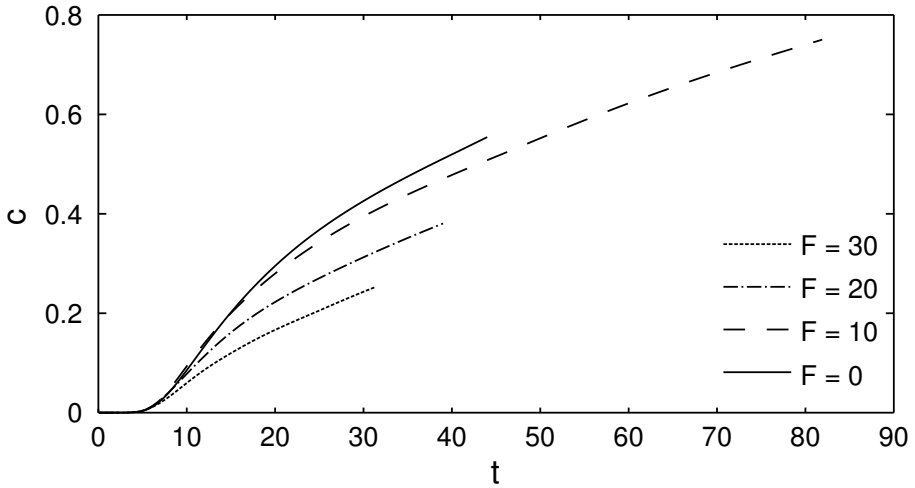

Fig. 6. Concentration value that undergoes inner splitting as a function function of time for $(M, Pe) = (3, 1000)$ and increasing values of F. Larger density differences lead to later inner splittings, even though we have stronger inner vorticity quadrupoles.

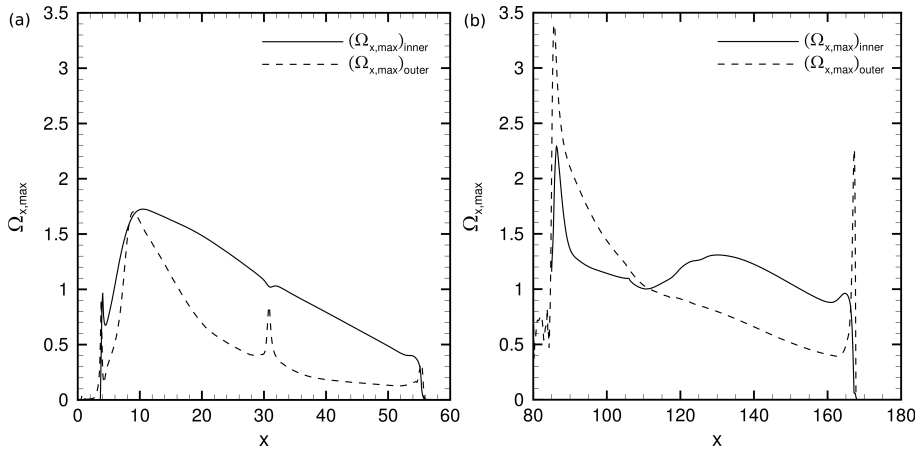

Fig. 7. Local maximum of the inner and outer vorticity quadrupoles, $(\Omega_{x,max}(x))_{inner}$ and $(\Omega_{x,max}(x))_{outer}$, respectively, as a function of the streamwise position for $(M,Pe) = (3,1000)$ at time $t = 30$ for (a) $F = 0$ and (b) $F = 30$. For $F = 30$, the stronger influence of the outer quadrupole counteracts the influence of the inner quadrupole, and contributes to a delayed inner splitting.

Taylor instability, which slows down the valleys connecting neighboring fingers, and eventually makes them reverse direction. This results in two opposite moving fronts that lead to the pattern seen in figure 5. The 'anchor'-like structure seen in the upstream moving front results from the interaction of the Rayleigh-Taylor instability with streamwise vorticity quadrupoles that contribute to 'carving' the anchor's flukes. In the upstream front, these quadrupoles act in a similar fashion to neutrally buoyant displacements discussed in the previous section and lead to the formation of the inner splitting event.

We have run simulations for $F = 0$, 10, 20 and 30. The formation of the anchor-like structure occurs for large values of the gravitational parameter F, and was only observed for the largest two values. Also, larger density differences lead to later inner splittings, even though we find stronger streamwise vorticity quadrupoles for larger F-values. Details of the first statement can be observed in figure 6 which depicts the concentration value at the moment it undergoes inner splitting as a function of time for increasing values of F. An explanation for the second statement is discussed in figure 7, which plots the local maximum of streamwise vorticity of the inner and outer quadrupoles, $(\Omega_{x,max}(x))_{inner}$ and $(\Omega_{x,max}(x))_{outer}$ for Pe = 1000, M = 3 at time t = 30 for (a) $F = 0$ and (b) $F = 30$. A stronger influence of the outer quadrupole for the $F = 30$ case counteracts the influence of the inner quadrupole and consequently the inner splittings develops later for larger F-values.

4.2. Horizontal displacements

In this configuration the flow no longer exhibits two planes of symmetry, as buoyancy makes the injected lighter fluid rise, approaching the top wall. Similar to the previous cases, we evolve the two-dimensional base state until time $t = 2$ before imposing a wavy spanwise perturbation. Figure 8 shows a perspective view of the $c = 0.5$ concentration isosurface for $(M,Re,Pe,F) = (2,1,2000,20)$ at time $t = 20$. While the top surface shows a pronounced, elongated cavity along $y = 0$ in the region $15 < x < 27$, no such cavity exists on the lower surface of the finger, which is gravitationally stable due to the presence of lighter fluid above denser fluid.

The origin of this cavity becomes clear from the $x = const.$ cross-cut shown in figure 9. This figure displays the concentration field (in gray shading) along with a projection of the velocity field onto the $x = const.$ plane. It demonstrates that the cavity formation is associated with a negatively buoyant plume of the denser fluid near $y = 0$, which is propelled downwards by a streamwise vortex dipole and thus bisects the finger lengthwise. This process is a clear manifestation of a Rayleigh-Taylor instability in the spanwise direction, as investigated in the linear stability analysis of Talon et al. [17]. Those authors show that a spanwise Rayleigh-Taylor instability along the upper side of a displacement front typically has a most amplified wavelength that is several times shorter than the dominant wavelength of the viscous fingering instability. Hence we expect to see more than one wavelength of the

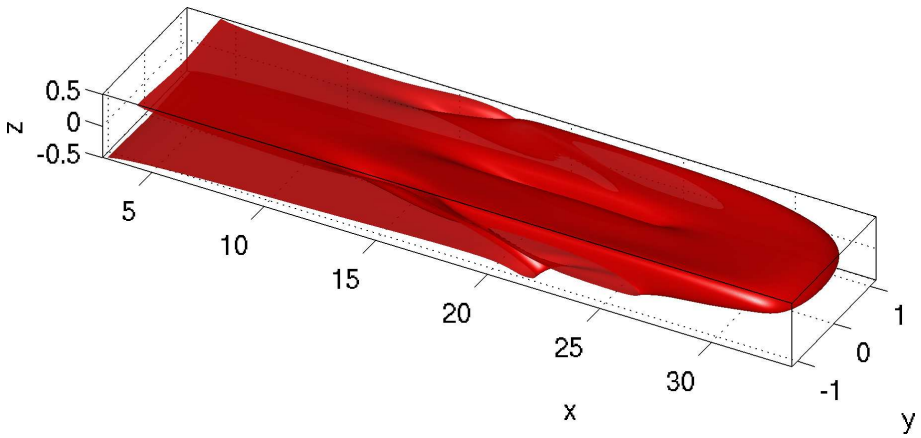

Fig. 8. Perspective view of the $c = 0.5$ concentration isosurface for $(M, Re, Pe, F) = (2, 1, 2000, 20)$ at time $t = 20$. Gravitational effects lead to the formation of a cavity structure that bisects the finger lengthwise.

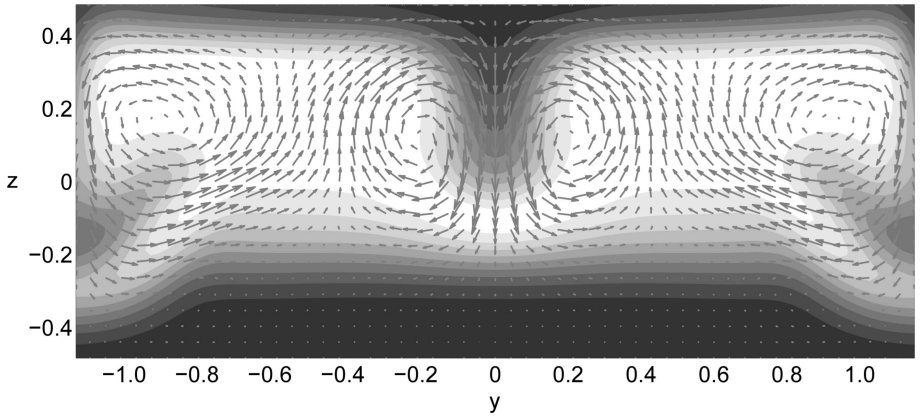

Fig. 9. Streamwise cross-section at $x = 22$ showing the concentration field in shades of gray, and the projection of the velocity field on this plane for the flow shown in figure 8. The inner cavity forms as a negatively buoyant plume sinks near $y = 0$, propelled by a vortex dipole.

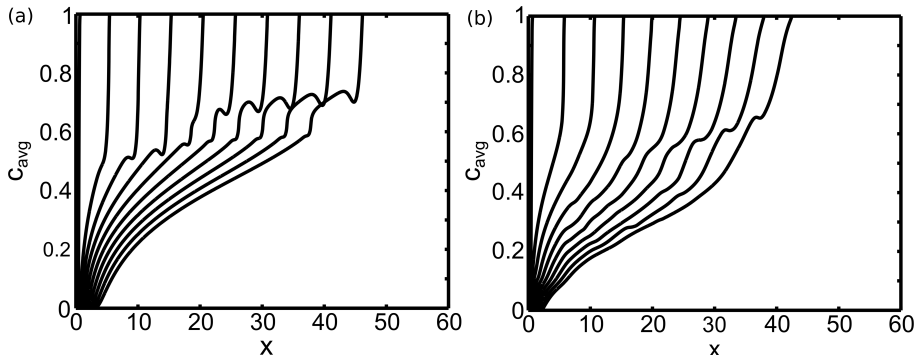

Fig. 10. Cross-section averaged concentration profiles for $(M, Re, Pe) = (2, 1, 2000)$ at times $t = 0$, 3, 6, …, 27 for (a) $F = 0$ and (b) $F = 60$. The variable density front propagates more slowly than the constant density one, indicating that a higher fraction of the resident fluid is being displaced in variable density flows.

Rayleigh-Taylor instability within one viscous fingering wavelength. This is consistent with the present observation of a Rayleigh-Taylor instability wavelength half as long as the viscous fingering instability wavelength, so that negatively buoyant plumes form at $y = -\lambda_m/2$, $y = 0$ and $y = \lambda_m/2$.

We remark that the present, gravitational splitting is fundamentally different from the inner splitting described earlier for constant density displacements. In those flows, a pronounced quadrupole streamwise vorticity structure forms which convects resident fluid from the walls to the center in a symmetric fashion, thereby resulting in a splitting event. When gravitational forces become important, this streamwise vorticity quadrupole gives way to the dipole structure near the center of the cell shown in figure 9, which leads to an asymmetric splitting. It appears possible that for flows such as the one shown in figure 8 these two splitting mechanisms may amplify each other, since the gravitational dipole structure is of the same sign and in approximately the same location as one half of the quadrupole structure in the constant density or vertical displacements. However, for other values of the governing parameters it may be possible that the ratio of the dominant Rayleigh-Taylor and viscous fingering instability wavelengths will be such that not one, but multiple cavities might form on the upper side of the front. For those cases, one would not expect the gravitational splitting to be amplified by the constant density inner splitting.

The gravitational splitting mechanism provides the dense fluid above the viscous finger with a more direct path to escape from the near wall region than having to move laterally all the way around the sides of the viscous finger. As the dense fluid from above the finger moves downward through the cavity, the buoyant viscous finger is able to rise towards the top wall into the space vacated by the dense fluid. That results in a sudden and rapid increase of the front elevation for different values of F. As expected, larger values of F result in earlier cavity formation, so that the dense fluid above the finger can escape more rapidly, and the front rises earlier. The front generally slows down as it rises and approaches the wall, which enhances the overall displacement efficiency.

This is shown in figure 10 which displays (y,z)-averaged concentration profiles for $(M,Re,Pe) = (2,1,2000)$ for the (a) neutrally buoyant case $F = 0$, while (b) shows the case for $F = 60$. Note that the intense mixing of the two fluids of the $F = 60$ case makes the three-dimensional front move significantly more slowly than for the corresponding neutrally buoyant case. This demonstrates the higher overall displacement efficiency of this case, indicating that the resident fluid is driven out of the Hele-Shaw cell more completely for variable density displacements than for neutrally buoyant ones. This observation is potentially significant for applications in enhanced oil recovery.

5. Conclusions

We have carried out three-dimensional simulations of the variable density and viscosity Navier-Stokes equations coupled to a convection-diffusion equation for the concentration field, in order to analyze miscible viscous fingering in a Hele-Shaw cell. We found that the dynamics in the direction perpendicular to the plane of the Hele-Shaw cell lead to the formation of a streamwise component of vorticity in the form of quadrupoles that bring fluid from the walls of the Hele-Shaw cell towards its center. This results in an inner splitting instability that splits the finger lengthwise.

The displacement of a viscous fluid by a lighter and less viscous one in the vertical direction results in a delayed inner splitting as the density contrast grows. Large values of the gravitational parameters also lead to a flow inversion in the valleys connecting neighboring fingers that result in opposite moving fronts. The interaction of the Rayleigh-Taylor instability with streamwise vorticity quadrupoles on the downward moving front can result in the formation of an 'anchor'-like structure.

In horizontal displacements, the injection of a lighter fluid breaks the up/down symmetry of the flow across the Hele-Shaw cell. Gravitational instabilities lead to the formation of a cavity that splits the finger lengthwise. This is consistent with results from linear stability analysis based on three-dimensional Stokes equations that predict smaller gravitational wavelengths than viscous wavelengths. The formation of this cavity is intrinsically different from the inner splitting mechanism, and the effects of these two can amplify each other contributing to the overall finger splitting. Large density differences also lead to better fluid mixing inside the finger and slower displacement fronts.

Acknowledgements

We are grateful to Felix Heussler and to Michael John for their help with the simulations described in section 4.
High-performance computing support was received through the California NanoSystems Institute under grant NSF

CHE-0321368, and through the Community Surface Dynamics Modeling System (CSDMS) facility at the University of Colorado in Boulder. We would like to thank CSDMS director Prof. James Syvitski and the technical staff at CSDMS for their support. E.M. acknowledges financial support through NSF grant CBET-0651498, DOE grant DE-FG02-08ER15991, and from the Petroleum Research Fund, administered by the American Chemical Society, under grant 45175-AC9. R.M.O would like to thank the CAPES Foundation in Brazil and the Fulbright program for financial support through grants BEX 2615/06-1 and IIE 15073695.

References

[1] Hill S. Channeling in packed columns. *Chem Eng Sci.* 1952;1:247–253.

[2] Saffman PG, Taylor GI. The penetration of a fluid into a porous medium or Hele-Shaw cell containing a more viscous liquid. *Proc R Soc London Ser A.* 1958;245:312–329.

[3] Homsy GM. Viscous fingering in porous media. *Annu Rev Fluid Mech.* 1987;19:271–311.

[4] Tryggvason G, Aref H. Numerical experiments on Hele-Shaw flow with a sharp interface. *J Fluid Mech.* 1983;136:1–30.

[5] Meiburg E, Homsy GM. Nonlinear unstable viscous fingers in Hele-Shaw flows. II. Numerical simulation. *Phys Fluids.* 1988;31(3):429–439.

[6] Tan CT, Homsy GM. Simulation of nonlinear viscous fingering in miscible displacement. *Phys Fluids.* 1988;31(6):1330–1338.

[7] Rogerson AM, Meiburg E. Numerical simulation of miscible displacement processes in porous media flows under gravity. *Phys Fluids A.* 1993;5(6):1344–1355.

[8] Chen CY, Meiburg E. Miscible porous media displacements in the quarter five-spot configuration. Part 1. The homogeneous case. *J Fluid Mech.* 1998;371:233–268.

[9] Chen CY, Meiburg E. Miscible porous media displacements in the quarter five-spot configuration. Part 2. Effect of heterogeneities. *J Fluid Mech.* 1998;371:269–299.

[10] Ruith M, Meiburg E. Miscible rectilinear displacements with gravity override. Part 1. Homogeneous porous medium. *J Fluid Mech.* 2000;420:225–257.

[11] McLean JW, Saffman PG. The effect of surface tension of the shape of fingers in a Hele-Shaw cell. *J Fluid Mech.* 1981;102:261–282.

[12] Pitts E. Penetration of fluid into a Hele-Shaw cell. *J Fluid Mech.* 1980;97:53–64.

[13] Goyal N, Meiburg E. Unstable density stratification of miscible fluids in a vertical Hele-Shaw cell: influence of variable viscosity on the linear stability. *J Fluid Mech.* 2004;516:211–238.

[14] Goyal N, Meiburg E. Miscible displacements in Hele-Shaw cells: two-dimensional base states and their linear stability. *J Fluid Mech.* 2006;558:329–355.

[15] Goyal N, Pichler H, Meiburg E. Variable-density miscible displacements in a vertical Hele-Shaw cell: linear stability. *J Fluid Mech.* 2007;584:357–372.

[16] Schafroth D, Goyal N, Meiburg E. Miscible displacements in HeleShaw cells: Nonmonotonic viscosity profiles. *Eur J Mech B/Fluids.* 2007;26:444–453.

[17] Talon L, Goyal N, Meiburg E. Variable density and viscosity, miscible displacements in horizontal Hele-Shaw cells. Part 1: Linear stability analysis. *In preparation.* 2012.

[18] Oliveira RM, Meiburg E. Miscible displacements in Hele-Shaw cells: three-dimensional Navier-Stokes simulations. *J Fluid Mech.* 2011;687:431–460.

Subject index

Author index